Biochar X

Original Research

Open Access

https://doi.org/10.48130/bchax-0025-0011

Lignin-derived carbon fibers loaded with NiO/Fe_3O_4 to promote oxygen evolution reaction

Xuezhi Zeng[1], Yutao Pan[1], Yi Qi[1], Yanlin Qin[1,2,3*] and Xueqing Qiu[1,2,3*]

Received: 26 July 2025

Revised: 6 October 2025

Accepted: 5 November 2025

Published online: 27 November 2025

Abstract

The sluggish kinetics and high overpotential of the oxygen evolution reaction (OER) remain key challenges limiting the efficiency of alkaline water electrolysis. Developing cost-effective, durable, and high-performance electrocatalysts from sustainable resources is therefore of great significance. Herein, we report a NiO/Fe_3O_4 heterojunction catalyst uniformly anchored on lignin-derived carbon fibers (NiO/Fe_3O_4@LCFs), synthesized via an integrated electrospinning–preoxidation–carbonization strategy using alkali lignin and PAN as dual carbon–nitrogen sources. The embedded NiO/Fe_3O_4 nanoparticles and nitrogen-doped carbon fiber network synergistically provide abundant active sites, rapid electron/ion transport, and strong structural stability. Benefiting from this architecture, NiO/Fe_3O_4@LCFs exhibits a low overpotential of 250 mV at 10 mA cm^{-2} and excellent durability with less than 10 mV degradation after 50 h at 100 mA cm^{-2}. The present approach demonstrates a scalable and renewable route to design efficient electrocatalysts by integrating biomass carbon supports with engineered bimetallic oxide interfaces, offering new insights for green energy conversion technologies.

Keywords: Electrospinning, Lignin carbon fibers, Spinel, Heterostructure interface, Oxygen evolution reaction

Highlights

- NiO/Fe_3O_4 nanoparticles embedded in N-doped lignin-derived carbon fibers (NiO/Fe_3O_4@LCFs).
- Co-action of embedded nanoparticles and conductive N-doped carbon network delivers abundant active sites, facilitated electron/ion transfer, and robust structural stability.
- NiO/Fe_3O_4 heterojunction accelerates OER kinetics via facilitated charge transfer, modulated d-band center, and balanced H_2O^*/O_2^* adsorption-desorption.

Graphical abstract

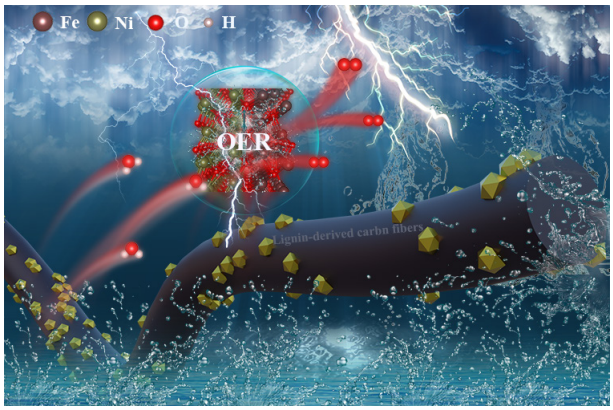

* Correspondence: Yanlin Qin (ylqin@gdut.edu.cn); Xueqing Qiu (qxq@gdut.edu.cn)

Full list of author information is available at the end of the article.

Introduction

The worldwide transition toward renewable power is intensifying the search for low-cost, earth-abundant electrocatalysts that can accelerate the oxygen-evolution reaction (OER)—the sluggish half-reaction that currently limits the efficiency of alkaline water-splitting and many metal–air batteries[1,2]. 4 e^-/4 H^+ transfer, adsorption of *OH/*O/*OOH intermediates and the concomitant lattice reconstruction all impose high kinetic barriers, so state-of-the-art noble-metal oxides (IrO_2, RuO_2) still outperform most base-metal alternatives[3]. Yet noble metals are scarce, geopolitically constrained and prone to dissolution at industrial current densities[4]. Consequently, mixed transition-metal (Ni, Co, Fe) oxides and (oxy)hydroxides have emerged as the most promising noble-metal-free OER catalysts because Ni^{2+}/Ni^{3+} redox couples furnish active γ-NiOOH species while Fe incorporation dramatically raises intrinsic activity by tuning the *OOH binding energy[5,6]. Nevertheless, these oxides suffer from low electronic conductivity, nanoparticle agglomeration, and mechanical pulverization under long-term oxygen bubbling, underscoring the need for an architected, conductive, and chemically robust scaffold[7–9].

To simultaneously resolve the trade-offs among conductivity, surface area, mechanical robustness, and cost, integrating transition-metal active phases with a conductive, yet robust support has become the mainstream strategy. Carbon scaffolds are considered ideal because of their high surface area, tailorable porosity, chemical inertness, and excellent electrical conductivity[10,11]. Nonetheless, traditional carbon carriers each have their own shortcomings: polyacrylonitrile-based carbon fibers offer high tensile strength but are limited by low specific surface areas and energy-intensive pre-oxidation/carbonization routines; CVD-grown carbon fibers provide precise structural control and high purity, yet their high energy demand, expensive equipment and low yield hinder scale-up; multi-walled carbon nanotubes possess outstanding conductivity and surface area, yet they readily agglomerate in electrolytes and bind catalysts only through weak physical adsorption, compromising long-term stability. Therefore, developing next-generation carbon supports that combine green processing, tunable architecture and strong interfacial coupling with metal phases remains essential[12,13].

Lignin, the most abundant renewable aromatic polymer on Earth, is primarily obtained as a low-value by-product from the paper and biorefinery industries, with an annual production of over 70 million tons[14–16]. Its intrinsic aromatic-rich structure and abundant functional groups make it a promising carbon precursor for the fabrication of high-performance porous carbon materials[17–19]. LCFs also confer several catalytic advantages that go beyond merely replacing fossil-based precursors. First, their disordered-graphitic microtexture and naturally high O/N/S heteroatom content create abundant defects, edge planes, and electron-rich sites that can anchor ultrafine metal/metal-oxide nanoparticles through covalent bonding or strong interfacial charge transfer, suppressing sintering at elevated potentials[20]. Second, the interconnected fiber network offers straight electronic highways and open macroporous channels, minimizing resistive drop while facilitating bubble detachment and electrolyte infiltration—two factors often overlooked in planar catalyst coatings[21]. Third, the life-cycle carbon footprint of LCFs production is estimated to be < 0.5 kg CO_2 eq kg^{-1}, an order of magnitude lower than that of PAN-based carbon fibers, directly aligning electrocatalyst fabrication with circular-bioeconomy principles[22,23]. Prior studies on Pt[24], Fe-N-C[25], and Co-Fe[26,27] nano-assemblies corroborate that lignin-derived carbon hosts can even improve turnover frequencies relative to commercial Vulcan carbon, attesting to the intrinsic catalytic synergy.

Compared with conventional synthetic carbon sources, such as polyacrylonitrile (PAN) or pitch, lignin offers significant advantages, including low cost, renewability, environmental friendliness, and structural versatility[28,29]. By utilizing lignin as a precursor, lignin-derived carbon fibers (LCFs) can be prepared via electrospinning or melt-spinning followed by carbonization. These carbon fibers exhibit a continuous one-dimensional morphology, high electrical conductivity, and hierarchical porous structures, which not only facilitate rapid electron transport but also provide abundant anchoring sites for the uniform dispersion of active nanoparticles[24,30]. Moreover, the fiber morphology enhances mechanical integrity and promotes better catalyst-electrolyte interaction, which is highly beneficial for improving catalytic durability and utilization efficiency[31].

Recent advances have demonstrated that combining transition metal oxides such as NiO and Fe_3O_4 with carbon supports can significantly enhance OER performance due to synergistic effects between metal sites and conductive matrices[32–35]. NiO possesses a high theoretical OER activity due to its ability to switch between Ni^{2+} and Ni^{3+} oxidation states during catalysis, which plays a crucial role in driving the OER intermediate formation and transformation steps[36,37]. Fe_3O_4, a mixed-valence iron oxide with excellent electronic conductivity and magnetic properties, has also been found to promote charge transport and modulate the electronic structure of Ni-based catalysts[38,39]. The incorporation of Ni into Fe-based systems can tune the local coordination environment, optimize the adsorption energy of reaction intermediates (such as *OH, *O, and *OOH), and thereby improve the intrinsic catalytic activity[40]. Despite the growing interest in using biomass-derived carbon materials for electrocatalysis, reports focusing on NiO/Fe_3O_4-decorated lignin-derived carbon fibers for OER applications remain scarce. Given the environmental and economic merits of lignin, along with the catalytic potential of Ni-Fe oxides, the rational construction of such a hybrid catalyst system is of considerable significance. It not only provides a sustainable route for the valorization of lignin waste but also introduces a new dimension to the design of low-cost, high-performance OER electrocatalysts.

In this study, a rational and scalable approach was designed to construct a lignin-derived carbon fiber-supported bimetallic oxide catalyst for enhanced OER performance. Lignin, polyacrylonitrile (PAN), and metal precursors (Ni^{2+}, Fe^{3+}) were co-dissolved in N,N-dimethylformamide (DMF), and processed via electrospinning to form uniform precursor fibers. This ensures homogeneous incorporation of metal ions into the lignin/PAN matrix. Through subsequent pre-oxidation and carbonization, NiO and spinel-structured Fe_3O_4 nanoparticles are *in situ* generated and uniformly embedded within the conductive carbon fiber network. The resulting NiO/Fe_3O_4@LCFs composite provides abundant active sites, improved electrical conductivity, and a robust three-dimensional architecture that facilitates rapid electron/ion transport during OER. To elucidate the structure–function relationship, detailed characterizations were conducted using SEM, TEM, XRD, XPS, and BET surface area analysis. These techniques confirm the uniform dispersion of metal oxides, formation of crystalline phases, and high porosity of the composite. Electrochemical measurements further demonstrate the catalyst's enhanced activity and durability in alkaline media, validating the effectiveness of this biomass-based hybrid architecture for oxygen evolution catalysis.

Materials and methods

Materials

Alkali lignin (AL) was supplied by Shandong Longli Biotechnology Co., Ltd. (Shandong, China), with an average molecular weight of 6,400 g mol^{-1}. Methanol (chromatography grade, ≥ 99.9%),

N,N-dimethylformamide (DMF, GC, > 99.9%), iron acetylacetonate (98%), nickel(II) acetylacetonate (95%), sodium hydroxide (NaOH, AR, 96%), and ethanol (C_2H_5OH, AR, moisture content ≤ 0.3%) were supplied by Shanghai Aladdin Bio-Chemical Technology Co., Ltd., China. Ammonium formate (ultra-pure, ≥ 99.0%), polyacrylonitrile (PAN, average Mw 150,000), and potassium hydroxide (KOH, 95%) were supplied by Shanghai Maclin Bio-Chemical Co., Ltd., China. Hydrochloric acid (HCl, AR), and acetone (AR) were purchased from Guangzhou Chemical Reagent Factory, China. Nafion solution (D520, 5 wt%) was provided by DuPont. Carbon paper (TGP-H-060, 20 × 20 cm, 0.19 mm) was produced by Toray Corporation (Japan). All chemicals were used as received without further purification.

Lignin treatment

First, 20 g of alkali lignin (AL) was dissolved in 250 mL of 1 M NaOH solution. The pH of the mixture was then adjusted to 12 using NaOH solution and stirred continuously at room temperature for 2 h. Subsequently, a dilute hydrochloric acid solution (pH = 2) was prepared and slowly added to the lignin solution until the pH dropped back to 2. The mixture was placed in an ice bath and allowed to react under continuous stirring for 2 h. It was then transferred to room temperature, and stirring was continued for 24 h to allow the lignin to fully precipitate and separate. The resulting precipitate was washed three times with the aforementioned dilute hydrochloric acid (pH = 2), and deionized water, respectively, and then centrifuged. Finally, the lignin sample obtained by centrifugation was freeze-dried for 24 h to obtain the final processed product.

Catalyst preparation

Iron acetylacetonate (0.706 g, 2 mmol), nickel acetylacetonate (0.262 g, 1 mmol), AL (1.673 g), and PAN (1.673 g) were dissolved in 20 mL of DMF, resulting in a polymer (AL and PAN) concentration of 15 wt% in DMF. The resulting solution was stirred at room temperature for 12 h to form a uniform spinning solution. The prepared spinning solution was then injected into a 5 mL syringe equipped with a 22 G stainless steel needle (inner diameter 0.70 mm, length 38 mm). Electrospinning was performed under the following conditions: a voltage of 19 kV, a needle tip-to-aluminum foil receiver distance of 12 cm, and a solution feed rate of 0.6 mL h^{-1}. The resulting lignin fibers were vacuum-dried at 60 °C for 24 h. The dried lignin fibers were then placed in a muffle furnace and pre-oxidized under an air atmosphere with the temperature raised from room temperature to 250 °C at a heating rate of 1 °C min^{-1}, and held at 250 °C for 1 h. Subsequently, the pre-oxidized thermally stabilized lignin fibers were transferred to a tube furnace and heated from room temperature to 800 °C under a nitrogen atmosphere at a rate of 3 °C min^{-1}, followed by isothermal treatment at 800 °C for 2 h to achieve carbonization. Next, the resulting lignin carbon fibers (LCFs) were placed in a muffle furnace and heated from room temperature to 300 °C at a rate of 2 °C min^{-1} under an air atmosphere, followed by isothermal treatment at 300 °C for 2 h, yielding the transition metal-loaded lignin carbon fiber catalyst, denoted as NiO/Fe_3O_4@LCFs. The Fe_3O_4@LCFs and NiO@LCFs catalysts were prepared using an identical procedure, with the only difference being the metal precursor used (iron acetylacetonate or nickel acetylacetonate, respectively), while all other steps remain unchanged. Structural characterisation parameters, electrochemical measurement methods, and density functional theory calculation method are detailed in Supplementary File 1.

Results and discussion

Synthesis and structural analysis of NiO/Fe_3O_4@LCFs catalyst

To prepare the lignin-derived carbon fibers (LCFs) catalyst, the precursor solution was first electrospun into a three-dimensional (3D) membrane composed of one-dimensional carbon nanofibers embedded with nickel and iron. Subsequently, pre-oxidation was performed to stabilize the microstructure and prevent fiber fusion during the following carbonization step. Finally, the material underwent thermal carbonization to form the NiO/Fe_3O_4@LCFs catalyst, featuring NiO/Fe_3O_4 nanoparticles anchored onto the lignin-derived carbon fibers (Fig. 1). As shown in Fig. 2, a series of microscopic characterizations were conducted to reveal the morphology, crystal structure, and elemental distribution of the NiO/Fe_3O_4@LCFs catalyst. Figure 2a, b show the low-magnification and high-magnification SEM images of NiO/Fe_3O_4@LCFs, respectively. The analysis results indicate that through electrospinning and subsequent carbonization processes, the lignin precursor was successfully converted into a carbon matrix (LCFs) with a fibrous morphology. Additionally, metal oxide (NiO/Fe_3O_4) particles are uniformly loaded onto these well-defined carbon fiber carriers. The catalyst exhibits a unique 'embedded' structural feature, where cubic-shaped metal oxide particles are firmly embedded within a relatively uniform carbon fiber network. Numerous nanoscale particles are uniformly distributed on the fiber surfaces, indicating successful spatial confinement of metal precursors during electrospinning and their subsequent in situ conversion to metal oxides during thermal treatment. TEM images in Fig. 2c, d further corroborate the SEM observations, clearly revealing the embedded structure of metal oxide particles on the LCFs carrier. TEM results indicate that the LCFs carrier provides an excellent dispersion platform for spinel-type metal oxide (NiO/Fe_3O_4) nanoparticles, suggesting strong interactions between the modified spinel nanoparticles and the carbon nanofiber carrier. Additionally, the high-resolution transmission electron microscopy (HRTEM) image of NiO/Fe_3O_4@LCFs (Fig. 2f)

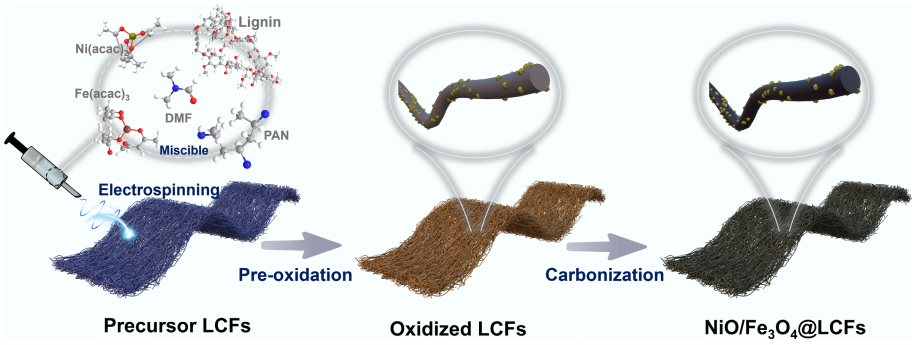

Fig. 1 Schematic diagram of the synthesis of NiO/Fe_3O_4@LCFs.

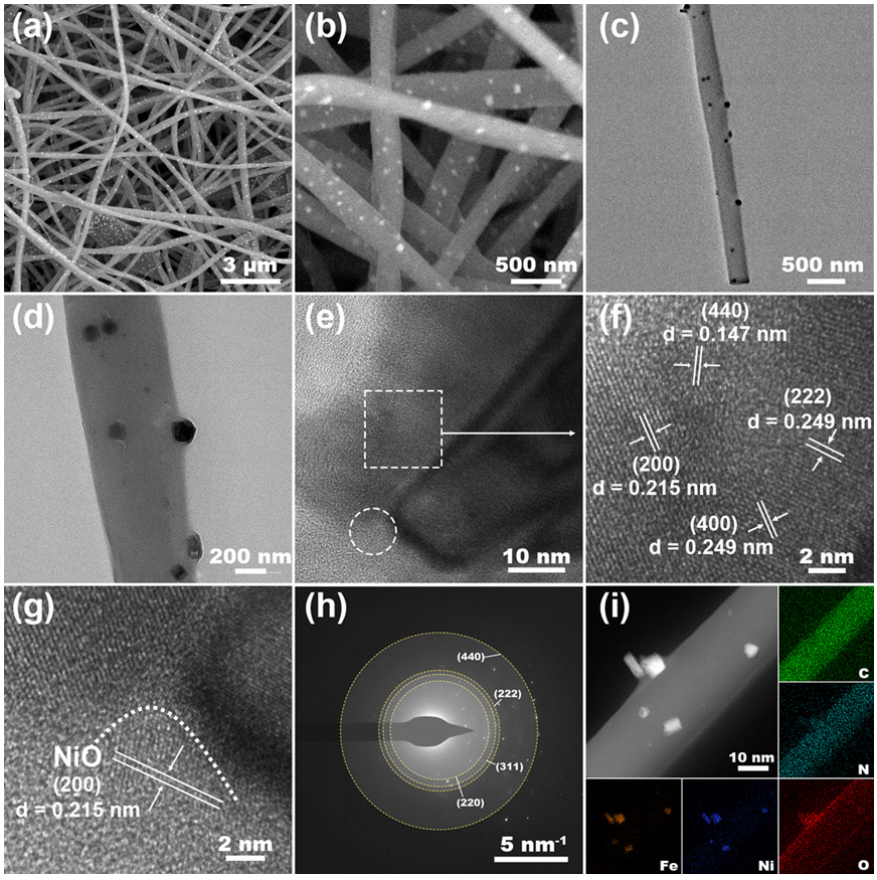

Fig. 2 Structural and elemental characterization of NiO/Fe_3O_4@LCFs: (**a**), (**b**) Low and high magnification SEM images of NiO/Fe_3O_4@LCFs; (**c**)–(**g**) TEM image, HRTEM image of NiO/Fe_3O_4@LCFs; (**h**) Electron diffraction pattern of NiO/Fe_3O_4@LCFs; (**i**) EDS elemental mapping images of C, N, O, Fe, and Ni elements.

successfully resolved the lattice fringes of the Fe_3O_4 spinel phase, clearly identifying its (511), (400), (440), and (311) crystal planes. Notably, a magnified observation of the region marked with a white circle in Fig. 2e shows that the lattice fringes in this region appear blurred (Fig. 2g), forming a distinct interface with the adjacent clear Fe_3O_4 spinel crystal plane regions. In the interfacial region (Fig. 2g), lattice distortion is observed, and the (200) plane of NiO is clearly resolved, demonstrating the formation of a nanoscale heterojunction between NiO and Fe_3O_4. This interface is expected to facilitate interfacial electron transfer and boost OER activity. The selected area electron diffraction (SAED) pattern shown in Fig. 2h further confirms the crystal structure of the Fe_3O_4 spinel phase, with diffraction rings corresponding to the (222), (220), (440), and (311) crystal planes. Elemental distribution information is provided by the energy-dispersive X-ray spectroscopy (EDS) surface scan pattern in Fig. 2i. The pattern clearly shows that C, O, and N elements exhibit highly uniform spatial distribution on the LCFs carrier, while Fe and Ni elements are primarily enriched in the embedded particle regions, further validating that metal particles are loaded onto the carbon fiber carrier in an embedded mode. It is worth emphasizing that the EDS results confirm the presence of abundant *in situ*-doped nitrogen (N) elements on the LCFs carrier, whose origin can be attributed to polyacrylonitrile (PAN) in the precursor. This *in situ* N doping not only significantly enhances the conductivity of carbon fibers but also improves the metal coordination ability of the catalyst by regulating the local electronic structure. Additionally, N doping effectively improves the inherently weak conductivity of the NiO/Fe_3O_4 spinel phase, thereby facilitating rapid electron transfer during the catalytic reaction and significantly enhancing the overall electrochemical performance of the catalyst[41,42]. In summary, this study successfully constructed an integrated catalyst (NiO/Fe_3O_4@LCFs) composed of cubic spinel-type metal oxide (NiO/Fe_3O_4) nanoparticles uniformly embedded in a nitrogen-doped carbon fiber (LCFs) carrier. Its unique embedded structure, heterojunction interface, and effective nitrogen doping synergistically form the foundation for the material's outstanding catalytic performance.

The structural composition of the catalyst was elucidated by X-ray diffraction (XRD) analysis (Fig. 3a). For Fe_3O_4@LCFs, the diffraction peaks appear at 30.1, 35.4, 37.1, 43.1, 53.4, 57.2, and 62.8°, corresponding to the (220), (311), (222), (400), (422), (511), and (440) crystal planes, confirming the presence of the Fe_3O_4 inverse spinel structure. In the XRD pattern of NiO/Fe_3O_4@LCFs, the characteristic peaks of Fe_3O_4, such as the (311), (440) characteristic peaks of Fe_3O_4, are also clearly observed in the XRD pattern of NiO/Fe_3O_4@LCFs. Notably, compared to Fe_3O_4@LCFs, the diffraction peak of the (400) crystal plane in NiO/Fe_3O_4@LCFs shifts to the left, indicating that some Ni may occupy part of the tetrahedral center sites in Fe_3O_4[43,44]. Additionally, NiO@LCFs exhibits a (200) diffraction peak attributable to NiO (PDF#47-1049). However, in both NiO@LCFs and NiO/Fe_3O_4@LCFs, the intensity of the NiO characteristic peaks is relatively weak, which may be due to the broad diffraction peaks of the amorphous carbon substrate masking some of the characteristic signals of the metal oxides[31]. Combining the above XRD results with the TEM observations of NiO and Fe_3O_4 forming a heterojunction and being embedded in the carbon fibers, it can be concluded that the NiO/Fe_3O_4@LCFs catalyst with a spinel structure loaded on

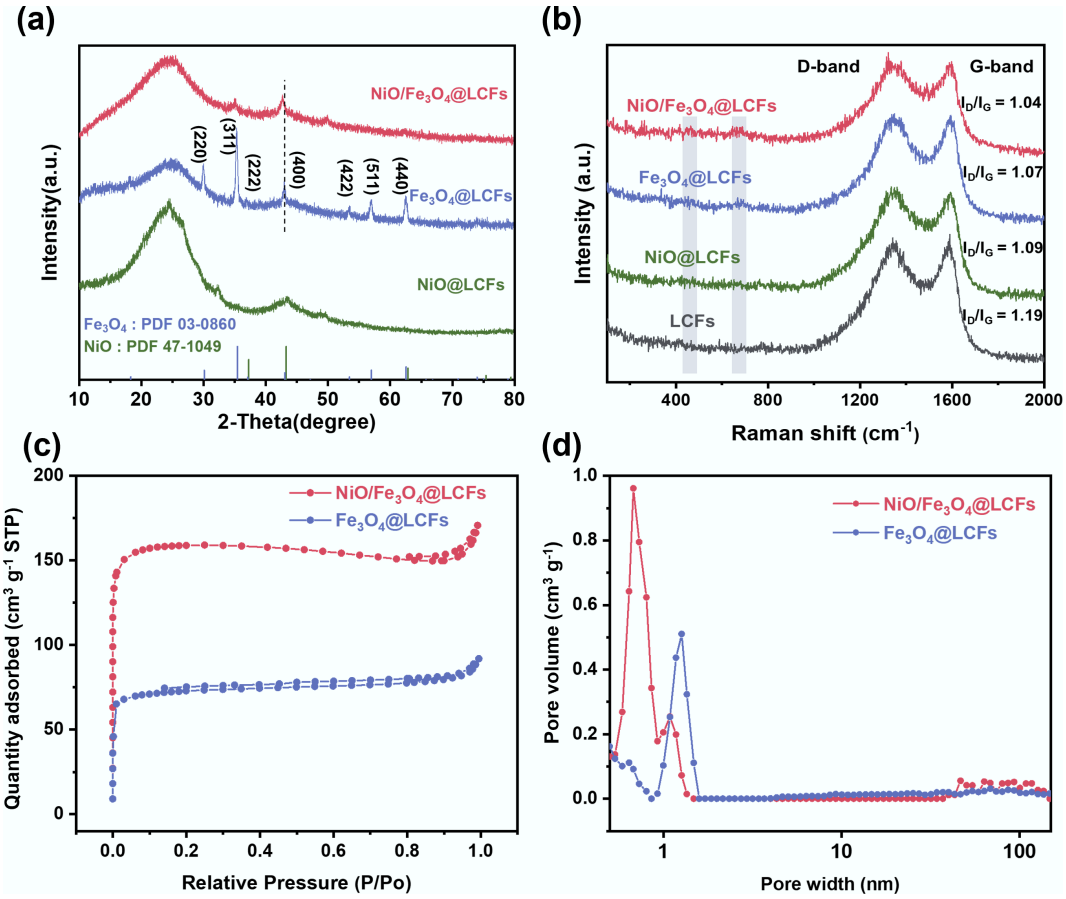

Fig. 3 Structural and physicochemical properties of the catalysts: (**a**) XRD patterns; (**b**) Raman spectra; (**c**) Specific surface area of Fe_3O_4@LCFs, NiO/Fe_3O_4@LCFs; (**d**) Pore size distribution of Fe_3O_4@LCFs, NiO/Fe_3O_4@LCFs.

lignin-based carbon fibers (LCFs) has been successfully synthesized. The interaction between the two metal oxides may play a significant role in enhancing the electrocatalytic-related physical properties of the material, such as electron transport.

Raman spectroscopy was used to assess the graphitization degree and defect characteristics of the catalyst's carbon matrix (Fig. 3b). Characteristic peaks were observed near ~1,350 cm^{-1} (D band) and ~1,580 cm^{-1} (G band) in all samples. The D band originates from sp^3-hybridized carbon, reflecting defects or disordered structures in the material; the G band originates from sp^2-hybridized carbon, representing ordered graphitized structures. The ratio of D band intensity to G band intensity (I_D/I_G) can be calculated to quantify the degree of disorder in the material. A higher I_D/I_G ratio indicates a greater contribution from defects or disordered structures in the material[45]. The I_D/I_G ratio of NiO/Fe_3O_4@LCFs (1.04) is lower than that of the metal-free (LCFs) and single-metal (NiO@LCFs and Fe_3O_4@LCFs) catalysts, indicating that the introduction of transition metal oxides (NiO, Fe_3O_4) effectively enhances the graphitization degree of the carbon matrix. This is attributed to the transition metal-catalyzed conversion of amorphous carbon to graphitized carbon, which may also improve the overall conductivity of the composite material[46]. Additionally, in the Raman spectra of metal-containing catalysts (NiO@LCFs, Fe_3O_4@LCFs, NiO/Fe_3O_4@LCFs), additional characteristic peaks appeared around 480 and 680 cm^{-1}, which were not observed in the absence of metal catalysts. These peaks correspond to the typical vibrational modes of Ni–O or Fe–O bonds, consistent with the detection of metal oxide phases in the XRD results.

Nitrogen (N_2) adsorption/desorption isotherms indicate that at a relative pressure (P/P_0) of 0.1, the isotherm rises, with NiO/Fe_3O_4@LCFs exhibiting the largest specific surface area (495 m^2 g^{-1}) (Fig. 3c and Supplementary Table S1). Additionally, the pore size distribution includes micropores and mesopores (Fig. 3d and Supplementary Table S1), and compared to Fe_3O_4@LCFs, NiO/Fe_3O_4@LCFs exhibits a larger pore structure. This pore structure facilitates electrolyte penetration, and provides a larger surface area for high-load active electrode materials[47]. Therefore, the reasonable structural design enables NiO/Fe_3O_4@LCFs to expose abundant active sites and exhibit rapid mass transfer pathways and high conductivity, thereby promoting rapid electrolyte penetration/diffusion and accelerating ion/electrolyte transport. It also guaranteed excellent electron conduction and allowed the generated O_2 to spread freely[48].

X-ray photoelectron spectroscopy (XPS) was used to analyze NiO@LCFs, Fe_3O_4@LCFs, and NiO/Fe_3O_4@LCFs to gain a deeper understanding of their surface valence states and chemical composition. The XPS spectra of NiO/Fe_3O_4@LCFs showed the presence of C, N, O, Fe, and Ni (Fig. 4a). In the Fe 2p spectrum, two subpeaks resulting from spin-orbit splitting indicate Fe^{3+} (725.2, 712.0 eV) and Fe^{2+} (723.1, 709.5 eV). Additionally, two broad peaks at 730.7 and 717.9 eV, were identified as typical satellite peaks (Sat.) of Fe 2p 1/2 and Fe 2p 3/2(Fig. 4b)[49,50]. Compared to Fe_3O_4@LCFs, the Fe 2p peaks of NiO/Fe_3O_4@LCFs are shifted 0.8 eV toward lower energy. This is because the introduction of Ni atoms may have occupied some of the tetrahedral sites originally occupied by Fe atoms,

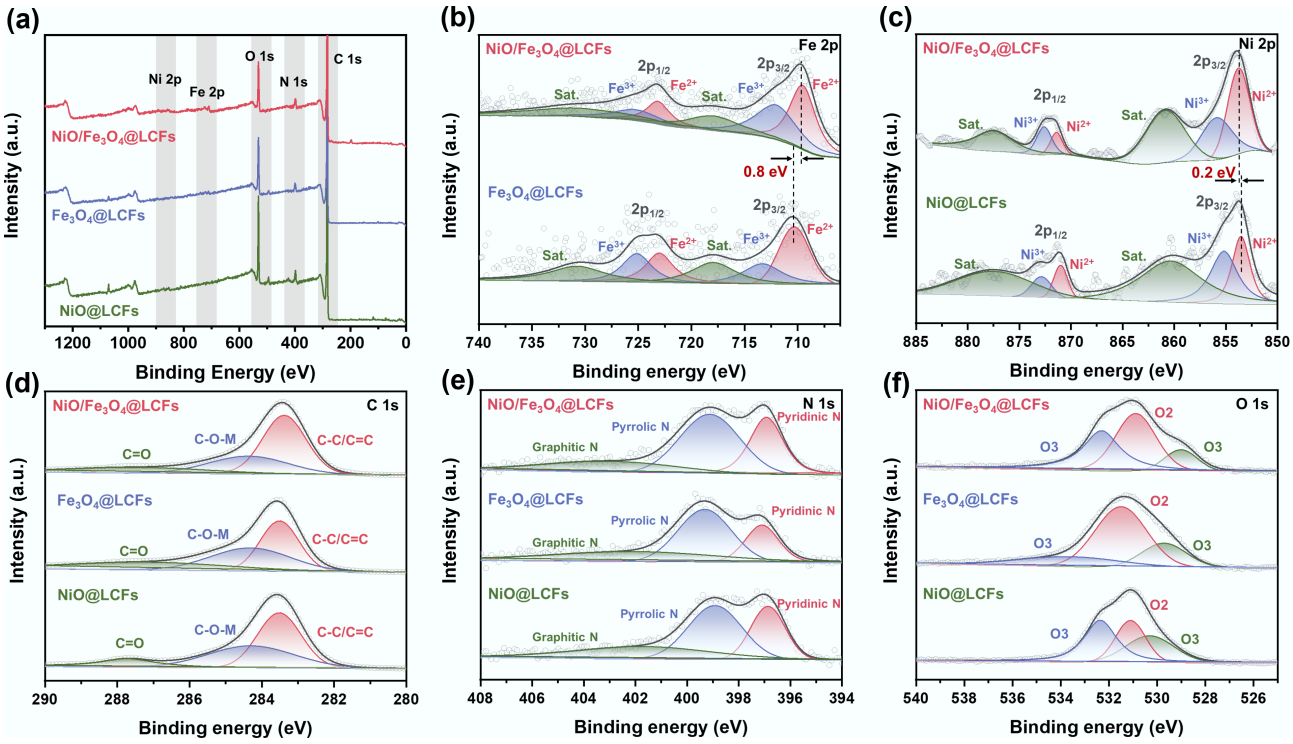

Fig. 4 XPS analysis of the surface composition and chemical states of NiO@LCFs, Fe_3O_4@LCFs, and NiO/Fe_3O_4@LCFs: (**a**) survey scan spectra; (**b**) Fe 2p; (**c**) Ni 2p; (**d**) C 1s; (**e**) N 1s; (**f**) O 1s.

leading to a reduction in Fe^{2+} content. This indicates that the introduction of Ni has caused a redistribution of charge structure in the spinel, consistent with the shift in XRD diffraction peak signals. The Ni 2p spectrum also exhibits similar characteristic peaks: Ni^{3+} (871.4 and 853.7 eV), and Ni^{2+} (872.6 and 855.9 eV) (Fig. 4c)[16]. Similarly, compared to NiO@LCFs, the Ni 2p spectrum exhibits a minor shift of 0.2 eV toward higher energies, indicating that the electronic structure of Ni in the Ni oxide has changed after the introduction of Fe_3O_4[51]. This alteration enhances electron transfer from Ni sites to Fe sites, leading to an increase in the content of high-valent Ni species—active sites for the oxygen evolution reaction (OER)—thereby improving electrocatalytic performance. These results reveal the coexistence of NiO and Fe_3O_4 spinel in the NiO/Fe_3O_4@LCFs catalyst.

In the C 1s spectrum (Fig. 4d), peaks at 283.4, 284.3, and 287.4 eV correspond to C=C/C–C, C–O–M, and C–O/C–N, respectively. This indicates successful carbonization of lignin, with lignin and PAN serving as the carbon and nitrogen sources for LCFs formation[31,52]. Fig. 4e shows the N 1s spectrum, which can be divided into three peaks at 396.9, 399.1, and 401.9 eV, corresponding to pyridine–N, pyrrole–N, and graphite–N, respectively[53–55]. Since pyridine–N is an electron-withdrawing group, it can adjust the local electronic structure of C. Compared to Fe_3O_4@LCFs, NiO/Fe_3O_4@LCFs has a higher content of pyridine–N with lone pair electrons, providing effective coordination sites with adjacent metal species, making it an effective electrocatalytic active site for OER[56]. Figure 4f shows the O 1s spectrum. At 529.0 eV, a distinct binding peak corresponding to oxygen atoms (O1) bound to metal can be observed. The peak at 531.0 eV is associated with defect sites of low-coordination oxygen (O2), while the peak at 532.3 eV indicates hydroxyl species adsorbed on the deoxidized surface (O3)[57] (Fig. 3f). Notably, the O 1s spectrum of NiO/Fe_3O_4@LCFs exhibits a distinct peak shift toward lower binding energies. The formation of the NiO/Fe_3O_4 heterostructure indicates strong electronic coupling between Ni, Fe, and O, further facilitating rapid electron transfer at the interface[58].

OER performance evaluation of NiO/Fe_3O_4@LCFs

In a 1.0 M KOH electrolyte, using a standard three-electrode system, the oxygen evolution reaction (OER) polarization curves of NiO/Fe_3O_4@LCFs and other reference catalysts were tested by linear sweep voltammetry (LSV) at a scan rate of 2 mV s^{-1}. Figure 5a shows the LSV curves of Fe_3O_4@LCFs, NiO@LCFs, and NiO/Fe_3O_4@LCFs. Compared to the single-metal oxide catalysts (NiO@LCFs and Fe_3O_4@LCFs), NiO/Fe_3O_4@LCFs exhibited the most outstanding OER electrocatalytic activity. This performance enhancement stems from the excellent electronic synergy between the two metal oxides, which effectively promotes the OER process. Figure 5b summarizes the overpotentials (η) at different current densities. At a current density of 10 mA cm^{-2}, the overpotentials of NiO@LCFs, Fe_3O_4@LCFs, and NiO/Fe_3O_4@LCFs are similar, at 250, 250, and 260 mV, respectively. However, at higher current densities (50 and 100 mA cm^{-2}), the overpotentials of NiO/Fe_3O_4@LCFs significantly decrease to 350 and 410 mV, respectively, showing a clear advantage over Fe_3O_4@LCFs (370, 440 mV) and NiO@LCFs (420 mV, 510 mV). The Tafel slope directly reflects the kinetics of the OER reaction, with smaller values indicating faster kinetics. The Tafel curves, calculated from the LSV curves, are shown in Fig. 5c. The Tafel slope of NiO/Fe_3O_4@LCFs (138 mV dec^{-1}) is significantly lower than that of NiO@LCFs (168 mV dec^{-1}), and Fe_3O_4@LCFs (144 mV dec^{-1}), further confirming that NiO/Fe_3O_4@LCFs exhibits faster OER reaction kinetics. As analyzed above, this kinetic advantage can be attributed to the synergistic interaction between the electronic and geometric structures of the bimetallic oxides. Additionally, electrochemical impedance spectroscopy (EIS) measurements revealed the intrinsic charge transfer characteristics of the catalyst. The Nyquist plot in Fig. 5d shows that the semicircle diameter (corresponding to the charge transfer resistance Rct) of NiO/Fe_3O_4@LCFs is

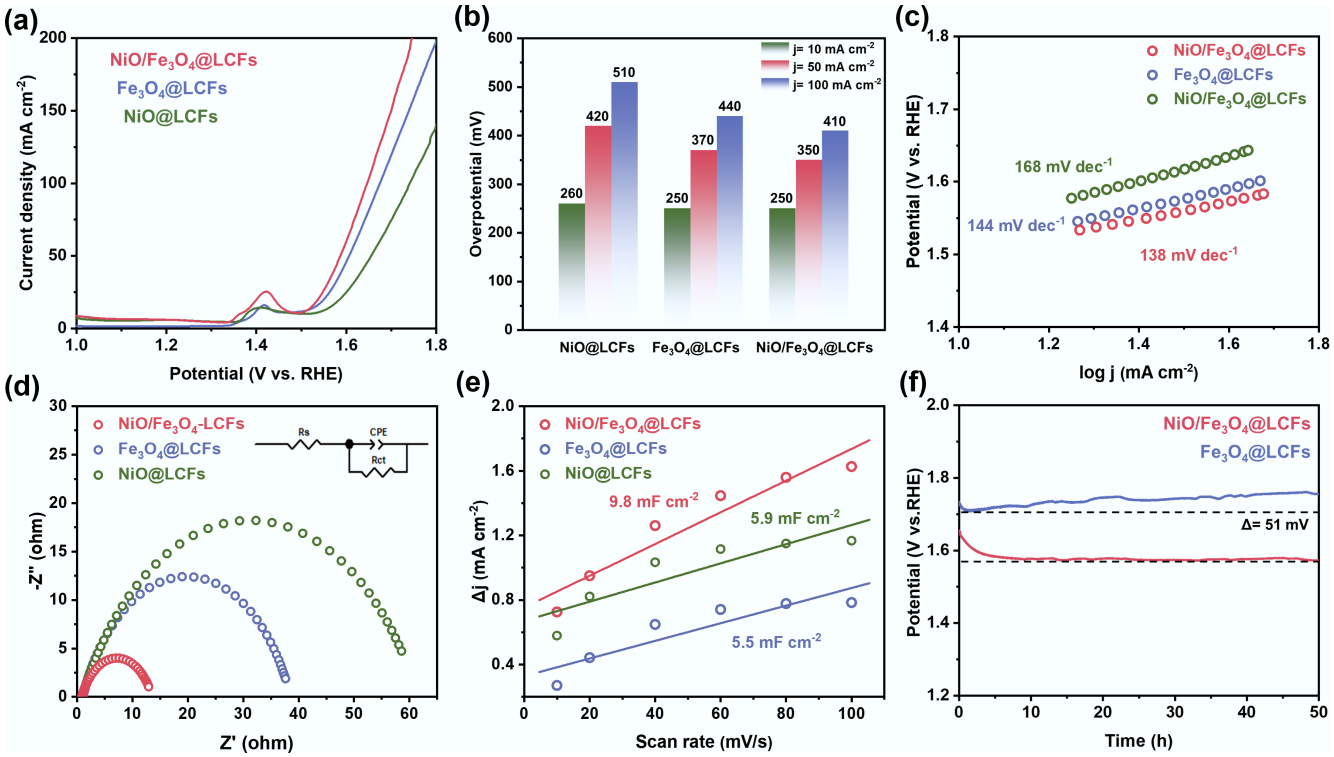

Fig. 5 Electrochemical properties of NiO@LCFs, Fe_3O_4@LCFs, and NiO/Fe_3O_4@LCFs: (**a**) LSV curves; (**b**) Overpotential required at j = 10, 50, and 100 mA cm^{-2}; (**c**) Tafel plots; (**d**) Nyquist plots; (**e**) Scan rate as a function of ECSA of bilayer capacitance; (**f**) Stability of Fe_3O_4@LCFs and NiO/Fe_3O_4@LCFs at a current density of 100 mA cm^{-2}.

significantly smaller than that of other catalysts. Based on equivalent circuit fitting, the Rct value of NiO/Fe_3O_4@LCFs is only 13.0 Ω, indicating faster charge transfer kinetics. Electrochemical surface area (ECSA) is an important indicator for evaluating the number of active sites on a catalyst, and it usually has a linear relationship with electrochemical double layer capacitance (Cdl)[59]. Cdl values were calculated via cyclic voltammetry (CV) testing at different scan rates (1.009 to 1.207 V vs RHE) (Fig. 5e and Supplementary Figs S1–S3). The Cdl of NiO/ Fe_3O_4@LCFs is 9.8 mF cm^{-2}, higher than that of Fe_3O_4@LCFs (5.9 mF cm^{-2}), and NiO@LCFs (5.5 mF cm^{-2}). This is primarily attributed to its high-surface-area porous structure, which provides a richer supply of active sites. The long-term stability of the catalyst is a critical indicator for practical applications. Chronopotentiometric testing was conducted at a high current density of 100 mA cm^{-2} (Fig. 5f). After 50 h of continuous operation, the operating voltage of Fe_3O_4@LCFs increased significantly by 51 mV, while the voltage of NiO/Fe_3O_4@LCFs remained largely stable, demonstrating excellent stability.

OER reaction mechanism on NiO/Fe_3O_4@LCFs catalyst

Understanding the reversible conversion of oxygen at atomic and molecular levels is crucial for elucidating catalytic reaction mechanisms. Figure 6a displays the in situ Raman spectra of NiO/Fe_3O_4@LCFs in 1 mol L^{-1} KOH electrolyte, clearly documenting the characteristic evolution of OER intermediates with potential. As the potential gradually increases, the positions and intensities of the bulk vibration peaks of NiO and Fe_3O_4 remain nearly unchanged, indicating no significant structural rearrangement in the metal oxide frameworks[57]. However, once the potential reaches 1.5 V (vs RHE), new Raman responses simultaneously emerge at 708, 808, 921, and 1,063 cm^{-1}. The peaks at 708 and 1,063 cm^{-1} correspond to the characteristic stretching vibrations of OH^- and $*O_2^-$ oxygen-containing intermediates, respectively, which continuously intensify and sharpen with increasing overpotential[60,61]. These results consistently indicate that the OER reaction follows an adsorption-evolution mechanism (AEM) pathway, wherein OH^-/$*O_2^-$ gradually accumulate on the catalyst surface and directly participate in the oxygen evolution process.

To corroborate the experimentally inferred AEM route, Fe_3O_4@LCFs and NiO/Fe_3O_4@LCFs models were constructed based on density functional theory (DFT) calculations. Stable adsorption configurations of key oxygen evolution reaction (OER) intermediates (OH, O, and OOH) were optimized, and their corresponding Gibbs free energy changes were calculated. The OER pathway follows the adsorption evolution mechanism (AEM): active sites first adsorb OH^- ions, which undergo deprotonation to form O; subsequent O–O bond coupling generates OOH; finally, O_2 molecules desorb from the catalyst surface via a second deprotonation. Moderate adsorption energy between oxygen intermediates and active sites facilitates OER kinetics[62].

The electronic structures of both models were analyzed. Bader charge calculations indicate electron transfer from NiO to Fe_3O_4 in NiO/Fe_3O_4@LCFs, increasing the charge on Fe and yielding an average valence state of +0.93, lower than that in Fe_3O_4@LCFs (+1.05)[43] (Supplementary Fig. S4). An additional 1.89 |e| flows from the N-doped lignin-derived carbon layer into the oxide cluster, further enriching the electron density of the active phase (Supplementary Fig. S5). This electronic structure change directly affects the d-band center position: as shown in Fig. 6b and Supplementary Figs S6–S8, the d-band center of Fe in Fe_3O_4@LCFs (–1.14 eV) is higher than that in NiO/Fe_3O_4@LCFs (–1.31 eV). Meanwhile, the d-band center of Ni in NiO/Fe_3O_4@LCFs is –1.59 eV, and the overall system d-band center is –1.49 eV. These results suggest that Ni introduction weakens the

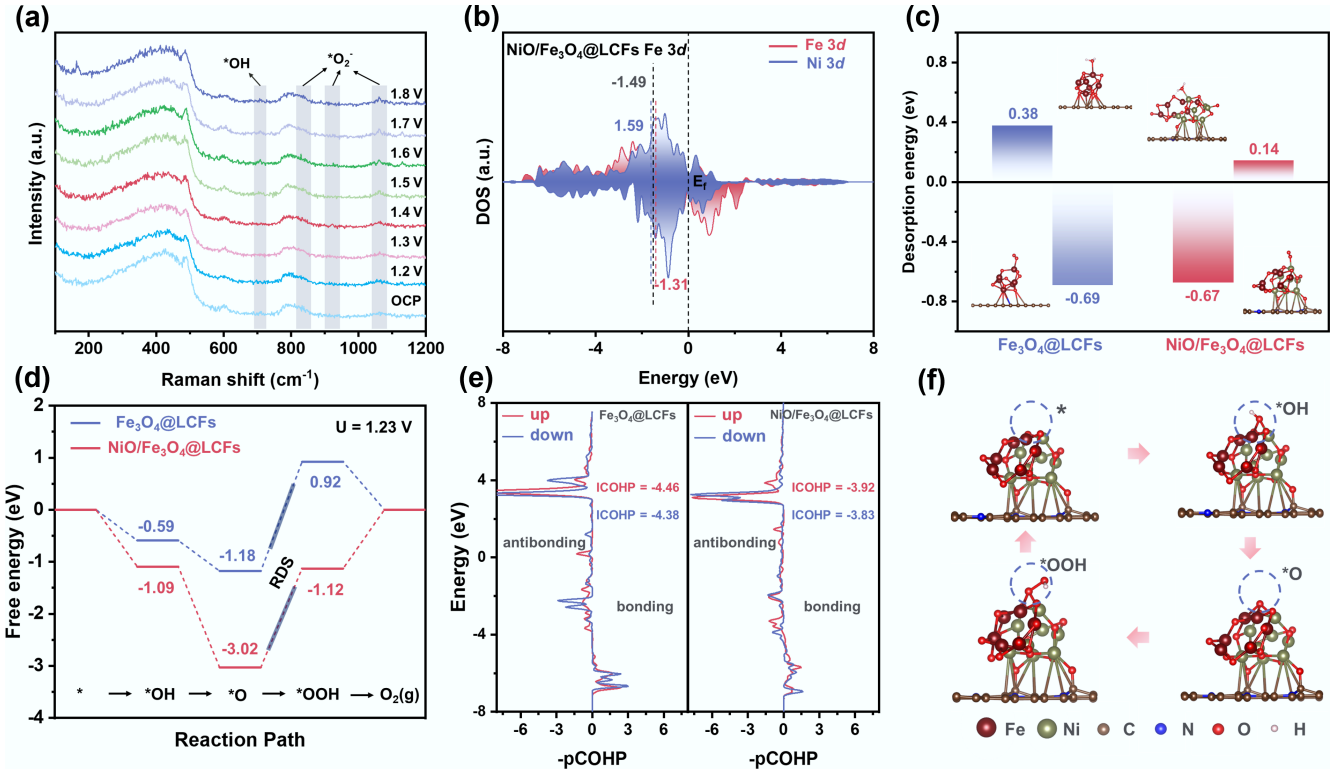

Fig. 6 Mechanistic insights into the enhanced OER activity via *in situ* spectroscopy and DFT calculations. (**a**) *In situ* Raman spectrum of the OER on NiO/Fe3O4@LCFs in 1.0 M KOH; (**b**) Density of states onto Fe and Ni 3d orbitals for NiO/Fe_3O_4@LCFs; (**c**) Adsorption energies of H_2O and O_2 on Fe_3O_4@LCFs and NiO/Fe_3O_4@LCFs; (**d**) Gibbs free energy change diagram of Fe_3O_4@LCFs, and NiO/Fe_3O_4@LCFs during the OER process; (**e**) The pCOHP plot of the O–OH bond after OOH adsorbs on Fe_3O_4@LCFs and NiO/Fe_3O_4@LCFs; (**f**) Interface configuration of NiO/Fe_3O_4@LCFs at four different stages during the OER.

adsorption strength of certain oxygen intermediates, as overly strong adsorption is detrimental to intermediate evolution[63]. The H_2O adsorption energy on both catalysts was calculated. The results showed a significantly higher H_2O adsorption energy on NiO/Fe_3O_4@LCFs than on Fe_3O_4@LCFs. Notably, H_2O primarily adsorbs on Ni sites, indicating that the NiO/Fe_3O_4 heterojunction promotes electron transfer, effectively activating Ni sites for H_2O adsorption. Meanwhile, O_2 adsorption energy on NiO/Fe_3O_4@LCFs is lower than on Fe_3O_4@LCFs, indicating easier O_2 desorption from the NiO/Fe_3O_4@LCFs surface. This optimized H_2O adsorption and O_2 desorption behavior collectively enhances the OER kinetics of NiO/Fe_3O_4@LCFs (Fig. 6c).

Figure 6d presents the OER free energy step diagrams for both catalysts. The rate-determining step (RDS) for both is *O → *OOH. Crucially, the RDS free energy change (ΔG_{RDS}) for NiO/Fe_3O_4@LCFs (1.9 eV) is significantly lower than that for Fe_3O_4@LCFs (2.1 eV), indicating superior OER activity of NiO/Fe_3O_4@LCFs. Bader charge and differential charge analysis further reveal that *OOH gains more electrons on NiO/Fe_3O_4@LCFs (0.42 |e| vs 0.35 |e| for Fe_3O_4@LCFs), signifying stronger interactions between *OOH and the NiO/Fe_3O_4@LCFs active sites (Supplementary Fig. S9). Crystal orbital Hamiltonian population (COHP) analysis of OOH interactions with both catalysts shows that for both spin-up and spin-down, the integrated COHP (ICOHP) values for the O–O bond in *OOH on NiO/Fe_3O_4@LCFs (–3.92 and –3.83) are greater (less negative) than those on Fe_3O_4@LCFs (–4.46 and –4.38) (Fig. 6e). This indicates a weaker O–O bond in *OOH on NiO/Fe_3O_4@LCFs, meaning the *O → *OOH step is more favorable, consistent with the reduced RDS energy barrier.

In summary, by studying the evolution of different intermediate configurations during OER (Fig. 6f), the NiO/Fe_3O_4@LCFs interface, with the lowest energy barrier, was identified as an efficient electroactive site. This interface allows optimal regulation for moderate adsorption of reaction intermediates and desorption of products.

Conclusions

In conclusion, a highly active and stable OER electrocatalyst has been developed—NiO/Fe_3O_4@LCFs—by embedding NiO and Fe_3O_4 nanoparticles within a nitrogen-doped lignin-derived carbon fiber matrix via electrospinning and controlled thermal treatment. Structural analysis confirmed the formation of spinel-phase metal oxides and the construction of a nanoscale NiO/Fe_3O_4 heterojunction, while EDS mapping and XPS revealed strong metal–carbon interactions and successful *in situ* nitrogen doping. The optimized NiO/Fe_3O_4@LCFs catalyst delivered superior electrochemical performance, including a low overpotential of 250 mV at 10 mA cm^{-2}, a small Tafel slope of 138 mV dec^{-1}, and a high double-layer capacitance of 9.8 mF cm^{-2}. Electrochemical impedance spectroscopy (EIS) further confirmed its low charge-transfer resistance, while chronoamperometric tests showed remarkable stability over 50 h with minimal voltage decay at 100 mA cm^{-2}. These results demonstrate that the combination of a renewable carbon fiber scaffold, *in situ*-formed bimetallic oxide heterojunctions, and nitrogen doping synergistically enhances the intrinsic activity and durability of the catalyst. This work offers a green and scalable strategy for designing next-generation biomass-based electrocatalysts for water splitting applications.

Supplementary information

It accompanies this paper at: https://doi.org/10.48130/bchax-0025-0011.

Author contributions

The authors confirm their contributions to the paper as follows: investigation: Zeng X, Pan Y, Qi Y, Qin Y; visualization: Zeng X, Qin Y, Qiu X; methodology: Pan Y, Qi Y; formal analysis: Pan Y, Qi Y, Qin Y, Qiu X; supervision: Qin Y, Qiu X; writing—review and editing: Zeng X; study design: Qiu X. All authors reviewed the results and approved the final version of the manuscript.

Data availability

The datasets used or analyzed during the current study are available from the corresponding author upon reasonable request.

Funding

This work was funded by the National Natural Science Foundation of China (22422802, U23A6005, and 22408057).

Declarations

Competing interests

The authors declare that they have no known competing financial interests or personal relationships that could have appeared to influence the work reported in this paper.

Author details

[1]Guangdong Provincial Key Laboratory of Plant Resources Biorefinery, School of Chemical Engineering and Light Industry, Guangdong University of Technology, Guangzhou 510006, China; [2]Guangdong Provincial Laboratory of Chemistry and Fine Chemical Engineering Jieyang Center, Jieyang 515200, China; [3]Guangdong Basic Research Center of Excellence for Ecological Security and Green Development, Guangdong University of Technology, Guangzhou 510006, China

References

[1] Hu C, Zhang L, Gong J. 2019. Recent progress made in the mechanism comprehension and design of electrocatalysts for alkaline water splitting. *Energy & Environmental Science* 12:2620–2645

[2] Lin Y, Tian Z, Zhang L, Ma J, Jiang Z, et al. 2019. Chromium-ruthenium oxide solid solution electrocatalyst for highly efficient oxygen evolution reaction in acidic media. *Nature Communications* 10:162

[3] Ghosh S, Basu RN. 2018. Multifunctional nanostructured electrocatalysts for energy conversion and storage: current status and perspectives. *Nanoscale* 10:11241–11280

[4] Li H, Zi X, Wu J, Wang X, Zhu L, et al. 2025. Plasmon-induced local electric field improved hydrogen evolution reaction on Ag/Mo_2C nanosheets. *Nano Research* 18:94907146

[5] Nai J, Xu X, Xie Q, Lu G, Wang Y, et al. 2022. Construction of $Ni(CN)_2/NiSe_2$ heterostructures by stepwise topochemical pathways for efficient electrocatalytic oxygen evolution. *Advanced Materials* 34:e2104405

[6] Zhai P, Wang C, Zhao Y, Zhang Y, Gao J, et al. 2023. Regulating electronic states of nitride/hydroxide to accelerate kinetics for oxygen evolution at large current density. *Nature Communications* 14:1873

[7] Yu M, Budiyanto E, Tüysüz H. 2022. Principles of water electrolysis and recent progress in cobalt-, nickel-, and iron-based oxides for the oxygen evolution reaction. *Angewandte Chemie* 61:e202103824

[8] Zhu K, Zhu X, Yang W. 2019. Application of *in situ* techniques for the characterization of NiFe-based oxygen evolution reaction (OER) electrocatalysts. *Angewandte Chemie International Edition* 58:1252–1265

[9] Hu F, Zhu S, Chen S, Li Y, Ma L, et al. 2017. Amorphous metallic NiFeP: a conductive bulk material achieving high activity for oxygen evolution reaction in both alkaline and acidic media. *Advanced Materials* 29:1606570

[10] Zhang L, Xiao J, Wang H, Shao M. 2017. Carbon-based electrocatalysts for hydrogen and oxygen evolution reactions. *ACS Catalysis* 7:7855–65

[11] Wang J, Kong H, Zhang J, Hao Y, Shao Z, et al. 2021. Carbon-based electrocatalysts for sustainable energy applications. *Progress in Materials Science* 116:100717

[12] Wang H, Li X, Jiang Y, Li M, Xiao Q, et al. 2022. A universal single-atom coating strategy based on tannic acid chemistry for multifunctional heterogeneous catalysis. *Angewandte Chemie* 134:e202200465

[13] Lin X, Liu J, Qiu X, Liu B, Wang X, et al. 2023. Ru–FeNi alloy heterojunctions on lignin-derived carbon as bifunctional electrocatalysts for efficient overall water splitting. *Angewandte Chemie International Edition* 62:e202306333

[14] Qi Y, Xiao X, Mei Y, Xiong L, Chen L, et al. 2022. Modulation of Brønsted and lewis acid centers for $Ni_xCo_{3-x}O_4$ spinel catalysts: towards efficient catalytic conversion of lignin. *Advanced Functional Materials* 32:2111615

[15] Qi Y, Liu B, Qiu X, Zeng X, Luo Z, et al. 2023. Simultaneous oxidative cleavage of lignin and reduction of furfural *via* efficient electrocatalysis by P-doped $CoMoO_4$. *Advanced Materials* 35:2208284

[16] Zeng X, Qi Y, Lin X, Li S, Qin Y. 2024. Ni modulates the coordination environment of cations in Fe_3O_4 to efficiently catalyze lignin depolymerization. *Chemical Engineering Science* 288:119798

[17] Moreno A, Sipponen MH. 2020. Lignin-based smart materials: a roadmap to processing and synthesis for current and future applications. *Materials Horizons* 7:2237–2257

[18] Sun SC, Xu Y, Wen JL, Yuan TQ, Sun RC. 2022. Recent advances in lignin-based carbon fibers (LCFs): precursors, fabrications, properties, and applications. *Green Chemistry* 24:5709–5738

[19] Jia G, Innocent MT, Yu Y, Hu Z, Wang X, et al. 2023. Lignin-based carbon fibers: Insight into structural evolution from lignin pretreatment, fiber forming, to pre-oxidation and carbonization. *International Journal of Biological Macromolecules* 226:646–659

[20] Liu J, Wu L, Chen D, Xu Q, Chen L, et al. 2024. Regulation engineering of lignin-derived N-doped carbon-supported FeNi alloy particles towards efficient electrocatalytic oxygen evolution. *Chemical Engineering Science* 285:119596

[21] Yan L, Liu H, Yang Y, Dai L, Si C. 2025. Lignin-derived carbon fibers: a green path from biomass to advanced materials. *Carbon Energy* 7:e662

[22] Zhang X, Dong S, Wu W, Yang J, Li J, et al. 2020. Influence of Lignin units on the properties of Lignin/PAN-derived carbon fibers. *Journal of Applied Polymer Science* 137:49274

[23] Qu W, Yang J, Sun X, Bai X, Jin H, et al. 2021. Towards producing high-quality lignin-based carbon fibers: a review of crucial factors affecting lignin properties and conversion techniques. *International Journal of Biological Macromolecules* 189:768–784

[24] García-Mateos FJ, Cordero-Lanzac T, Berenguer R, Morallón E, Cazorla-Amorós D, et al. 2017. Lignin-derived Pt supported carbon (submicron)fiber electrocatalysts for alcohol electro-oxidation. *Applied Catalysis B: Environmental* 211:18–30

[25] Qu X, Yang Y, Dong L, Li Z, Feng Y, et al. 2024. Enzymolytic lignin derived Fe–N codoped porous carbon materials as catalysts for oxygen reduction reactions. *Biomass and Bioenergy* 184:107173

[26] Lin X, Liu J, Wu L, Chen L, Qi Y, et al. 2022. *In situ* coupling of lignin-derived carbon-encapsulated CoFe-CoxN heterojunction for oxygen evolution reaction. *AIChE Journal* 68:e17785

[27] Zhang J, Liu J, Ran J, Lin X, Wang H, et al. 2025. Oxidative ammonolysis modified lignin-derived nitrogen-doped carbon-supported Co/Fe composites as bifunctional electrocatalyst for Zn-air batteries. *Chinese Chemical Letters* 36:110403

[28] Jia G, Yu Y, Wang X, Jia C, Hu Z, et al. 2023. Highly conductive and porous lignin-derived carbon fibers. *Materials Horizons* 10:5847–5858

[29] Chatterjee S, Saito T. 2025. Lignin-derived advanced carbon materials. *ChemSusChem* 8(23):3941–3958

[30] Jia G, Zhou Z, Wang Q, Innocent MT, Wang S, et al. 2022. Effect of pre-oxidation temperature and heating rate on the microstructure of lignin carbon fibers. *International Journal of Biological Macromolecules* 216:388–396

[31] Wu H, Liu B, Qi Y, Qiu X, Chen L, et al. 2024. High-conductivity lignin-derived carbon fiber-embedded $CuFe_2O_4$ catalysts for electrooxidation of HMF into FDCA. *ACS Catalysis* 14(21):16127–16139

[32] Davis EM, Bergmann A, Kuhlenbeck H, Roldan Cuenya B. 2024. Facet dependence of the oxygen evolution reaction on Co_3O_4, $CoFe_2O_4$, and Fe_3O_4 epitaxial film electrocatalysts. *Journal of the American Chemical Society* 146:13770–13782

[33] Zhang H, Jiang Z, Wu C, Xi S, Song J, et al. 2025. Fe-redox-oriented electrochemical activation strategy enabling enhancement for efficient oxygen evolution reaction. *Chem Catalysis* 5:101196

[34] Luong TN, Doan TLL, Bacirhonde PM, Park CH. 2025. A study on synthesis of an advanced electrocatalyst based on high-conductive carbon nanofibers shelled $NiFe_2O_4$ nanorods for oxygen evolution reaction. *International Journal of Hydrogen Energy* 99:1108–1118

[35] Li C, Ye B, Ouyang B, Zhang T, Tang T, et al. 2025. Dual doping of N and F on Co_3O_4 to activate the lattice oxygen for efficient and robust oxygen evolution reaction. *Advanced Materials* 37:2501381

[36] Aman S, Ahmad N, Tahir MB, Alanazi MM, Abdelmohsen SAM, et al. 2023. Understanding the spatial configurations of Sm_2O_3 in NiO interfaces Embedded-Loaded for Electrocatalytic OER process. *Surfaces and Interfaces* 38:102857

[37] da Silva GL, da Silva Hortêncio J, de Souza Soares JPG, de Almeida Lourenço A, Raimundo RA, et al. 2024. *Phyto*-assisted green synthesis of NiO nanoparticles for OER electrocatalysis. *International Journal of Hydrogen Energy* 80:308–321

[38] Pawar AA, Bandal HA, Kim H. 2021. Spinel type Fe_3O_4 polyhedron supported on nickel foam as an electrocatalyst for water oxidation reaction. *Journal of Alloys and Compounds* 863:158742

[39] Ye L, Zhu P, Wang T, Li X, Zhuang L. 2023. High-performance flower-like and biocompatible nickel-coated $Fe_3O_4@SiO_2$ magnetic nanoparticles decorated on a graphene electrocatalyst for the oxygen evolution reaction. *Nanoscale Advances* 5:4852–4862

[40] Li CF, Xie LJ, Zhao JW, Gu LF, Tang HB, et al. 2022. Interfacial Fe–O–Ni–O–Fe bonding regulates the active Ni sites of Ni-MOFs *via* iron doping and decorating with FeOOH for super-efficient oxygen evolution. *Angewandte Chemie International Edition* 61:e202116934

[41] Liu X, Park M, Kim MG, Gupta S, Wu G, et al. 2015. Integrating NiCo alloys with their oxides as efficient bifunctional cathode catalysts for rechargeable zinc–air batteries. *Angewandte Chemie International Edition* 54:9654–9658

[42] Wang Q, Shang L, Shi R, Zhang X, Zhao Y, et al. 2017. NiFe layered double hydroxide nanoparticles on co, N-codoped carbon nanoframes as efficient bifunctional catalysts for rechargeable zinc–air batteries. *Advanced Energy Materials* 7:1700467

[43] Xu W, Zhong W, Yang C, Zhao R, Wu J, et al. 2022. Tailoring interfacial electron redistribution of Ni/Fe_3O_4 electrocatalysts for superior overall water splitting. *Journal of Energy Chemistry* 73:330–338

[44] Halder J, De P, Mandal D, Chandra A. 2023. Bricks of Co, Ni doped Fe_3O_4 as high performing pseudocapacitor electrode. *Journal of Energy Storage* 58:106391

[45] Tan Y, Zhu W, Zhang Z, Wu W, Chen R, et al. 2021. Electronic tuning of confined sub-nanometer cobalt oxide clusters boosting oxygen catalysis and rechargeable Zn–air batteries. *Nano Energy* 83:105813

[46] Tao X, Xu H, Luo S, Wu Y, Tian C, et al. 2020. Construction of N-doped carbon nanotube encapsulated active nanoparticles in hierarchically porous carbonized wood frameworks to boost the oxygen evolution reaction. *Applied Catalysis B: Environmental* 279:119367

[47] Gan W, Wu L, Wang Y, Gao H, Gao L, et al. 2021. Carbonized wood decorated with cobalt-nickel binary nanoparticles as a low-cost and efficient electrode for water splitting. *Advanced Functional Materials* 31:2010951

[48] Chen Z, Zhuo H, Hu Y, Lai H, Liu L, et al. 2020. Wood-derived lightweight and elastic carbon aerogel for pressure sensing and energy storage. *Advanced Functional Materials* 30:1910292

[49] Yamashita T, Hayes P. 2008. Analysis of XPS spectra of Fe^{2+} and Fe^{3+} ions in oxide materials. *Applied Surface Science* 254:2441–2449

[50] Jaffari GH, Rumaiz AK, Woicik JC, Shah SI. 2012. Influence of oxygen vacancies on the electronic structure and magnetic properties of $NiFe_2O_4$ thin films. *Journal of Applied Physics* 111:093906

[51] Ryan PTP, Jakub Z, Balajka J, Hulva J, Meier M, et al. 2018. Direct measurement of Ni incorporation into $Fe_3O_4(001)$. *Physical Chemistry Chemical Physics* 20:16469–16476

[52] Zhang J, Zhang J, He F, Chen Y, Zhu J, et al. 2021. Defect and doping co-engineered non-metal nanocarbon ORR electrocatalyst. *Nano-Micro Letters* 13:65

[53] Su Y, Jiang H, Zhu Y, Yang X, Shen J, et al. 2014. Enriched graphitic N-doped carbon-supported Fe_3O_4 nanoparticles as efficient electrocatalysts for oxygen reduction reaction. *Journal of Materials Chemistry A* 2:7281–7287

[54] Zhang H, Liao JJ, Chen L, Chen XY, Yu ZP, et al. 2025. Low-amount RuP2 nanocluster anchored on P, N-codoped carbon with optimized H and H_2O adsorption boost hydrogen evolution in anion-exchange membrane water electrolyzer. *Rare Metals* 44:6268–6278

[55] Zhang H, Chen A, Bi Z, Wang X, Liu X, et al. 2023. MOF-on-MOF-derived ultrafine Fe_2P-Co_2P heterostructures for high-efficiency and durable anion exchange membrane water electrolyzers. *ACS Nano* 17:24070–24079

[56] Balamurugan J, Austeria PM, Kim JB, Jeong ES, Huang HH, et al. 2023. Electrocatalysts for zinc–air batteries featuring single molybdenum atoms in a nitrogen-doped carbon framework. *Advanced Materials* 35:2302625

[57] Chen X, Qi Y, Liu B, Qiu X, Lin X, et al. 2025. Structural optimization of the $NiFe_2O_4$ spinel catalyst aimed at efficient electrocatalytic C-O bond cleavage of lignin. *Chemical Engineering Science* 301:120722

[58] Zhou L, Li J, Yin J, Zhang G, Zhang P, et al. 2024. Heterostructure catalyst coupled wood-derived carbon and cobalt-iron alloy/oxide for reversible oxygen conversion. *Biochar* 6:54

[59] Hu X, Zhang S, Sun J, Yu L, Qian X, et al. 2019. 2D Fe-containing cobalt phosphide/cobalt oxide lateral heterostructure with enhanced activity for oxygen evolution reaction. *Nano Energy* 56:109–17

[60] Luo N, Cai A, Pei J, Zeng X, Wang X, et al. 2025. Unveiling oxygen vacancy engineering in CoMo-based catalysts for enhanced oxygen evolution reaction activity. *Advanced Functional Materials* 35:2425503

[61] Xin S, Tang Y, Jia B, Zhang Z, Li C, et al. 2023. Coupling adsorbed evolution and lattice oxygen mechanism in Fe-co$(OH)_2/Fe_2O_3$ heterostructure for enhanced electrochemical water oxidation. *Advanced Functional Materials* 33:2305243

[62] Wang X, Xi S, Huang P, Du Y, Zhong H, et al. 2022. Pivotal role of reversible NiO_6 geometric conversion in oxygen evolution. *Nature* 611:702–708

[63] Gao L, Cui X, Sewell CD, Li J, Lin Z. 2021. Recent advances in activating surface reconstruction for the high-efficiency oxygen evolution reaction. *Chemical Society Reviews* 50:8428–8469